Available online at www.sciencedirect.com
SCIENCE DIRECT®
International Journal of Heat and Fluid Flow 26 (2005) 440–458
International Journal of HEAT AND FLUID FLOW
www.elsevier.com/locate/ijhff

Experimental and numerical investigation of the flow field through a heat exchanger for aero-engine applications

D. Missirlis [a], K. Yakinthos [a], A. Palikaras [a], K. Katheder [b], A. Goulas [a,*]

[a] *Laboratory of Fluid Mechanics and Turbomachinery, Department of Mechanical Engineering, Aristotle University of Thessaloniki, Thessaloniki 54 124, Greece*
[b] *MTU Aero Engines GmbH, Munich, Germany*

Received 19 April 2004; accepted 11 October 2004
Available online 26 November 2004

Abstract

An experimental and computational study for the flow development through a heat exchanger for aero-engine applications is presented. The heat exchanger consists of elliptic tubes in a U formation, the ends of which are attached to the collector pipe, which has a cylindrical cross section. In this way, two identical packages (named as matrices) are formed and located at a certain distance between them. The elliptic tubes are placed in a staggered arrangement. Detailed flow measurements using a 3-hole pitot-static probe were carried out on a 1:1 scale model of the heat exchanger in order to measure the pressure drop through the heat exchanger and the velocity distribution behind it. The flow through the heat exchanger was modeled with a computational fluid dynamics approach. The heat exchanger matrices were modeled using a porous medium assumption. The pressure drop through each element of the porous medium was linked to an effective local velocity. In order to check the validity of the computational modeling, the results were compared to the measured flow parameters such as pressure and velocity distributions. Two sets of modeling were performed assuming a laminar and a turbulent flow. The results showed that the laminar approach gave better results and this is supported by the corresponding Reynolds numbers, which indicated that the global flow field is transitional.
© 2004 Elsevier Inc. All rights reserved.

Keywords: Heat exchanger; Flow field; Aero-engine applications; Porous media; Turbulence modeling; Experimental and numerical investigation

1. Introduction

In the past, work has been carried out concerning the flow development through heat exchangers mainly on the comparison of the effects of tube geometry. Comparative studies have been carried out between tubes having elliptic and circular cross section on the basis of pressure loss and heat transfer performance. In most cases better results for staggered banks of finned elliptic tubes submitted to a cross-flow free stream were reported, Boetler et al. (1949); Brauer (1964); Schulenberg (1966); Bordalo and Saboya (1999); Saboya and Saboya (2001); Rocha et al. (1997). Numerical studies concerning the optimization procedure for tube positioning inside the heat exchanger have also been presented, Matos et al. (2001). An optimum geometric arrangement for circular and elliptic tubes was found and it was demonstrated to give maximum heat transfer for various Reynolds numbers.

A limited work has been carried out concerning the flow development downstream the tube banks, which affects the pressure losses through a heat exchanger. A study for the formulation of von Karman vortices in staggered tube bundles has been carried out by Umeda and Yang (1999), where flow visualization, LDA velocity measurements and pressure drop measurements have been carried out to obtain a detailed description of the

* Corresponding author. Tel.: +30 2310 996001; fax: +30 2310 996410.
E-mail address: goulas@eng.auth.gr (A. Goulas).

0142-727X/$ - see front matter © 2004 Elsevier Inc. All rights reserved.
doi:10.1016/j.ijheatfluidflow.2004.10.003

Nomenclature

A	heat exchanger total heat transfer area
A_{fr}	heat exchanger total frontal area
c_μ	constant for the turbulence modeling
$C_{p\,yaw}$	dimensionless probe calibration coefficient for yaw angle
d	characteristic length for the definition of the Reynolds number
f	friction factor
g	proportionality factor in Newton's second law
H	spanwise distance of wind-tunnel
k	turbulence kinetic energy
L	flow length of the heat exchanger tubes
l	characteristic turbulent length scale
m	mass flow
P_1, P_2	pressure of probe side holes 1 and 2
P_3	pressure of probe center hole
P_{ave}	average pressure of probe side holes 1 and 2
P_{ref}	average airflow static pressure at the inlet section of the computational domain
P_{static}	static pressure
P_{total}	total pressure
p	average porosity of the matrix surface, dimensionless
Q_p, S_p	dimensionless probe calibration coefficients
Re	Reynolds number
r_h	hydraulic radius of the heat exchanger
T_u	turbulence intensity level
V_{max}	average maximum velocity through the gap between the tubes
V	airflow velocity
V_{eff}	airflow effective velocity
V_{ref}	average streamwise airflow velocity at the inlet section of the computational domain
$V_{x-effective}$	average streamwise effective airflow velocity for the straight part region of the heat exchanger
V_{x-mean}	average streamwise airflow velocity for the straight part region of the heat exchanger
v	kinematic viscosity
v_{inlet}	specific volume at the inlet side of the heat exchanger
v_{inlet}	specific volume at the outlet side of the heat exchanger
v_m	mean specific volume
y^+	dimensionless local normal distance from the wall

Greek symbols

ΔP	static pressure drop
ε	turbulence dissipation rate
μ	dynamic viscosity
ρ	density
ρ_{inlet}	average density of air at the inlet side of the heat exchanger
ρ_{inlet}	average density of air at the outlet side of the heat exchanger

flow development for a range of Reynolds numbers. It was shown that the staggered arrangement of the tubes and the Reynolds number affect the shape and the size of the wake behind the tubes. Additionally, it was shown that these parameters affect also the friction loss coefficients. Bouris et al. (2001), presented a numerical evaluation of the heat transfer mechanism of alternative tube configurations in a heat exchanger, where they concluded that the use of elliptic shape tubes gives increased heat transfer rates, because the lower pressure drop imposed by the shape of the tube, allows tubes to be placed at closer spacing. Finally, Goulas et al. (2003) presented experimental data and computational results for a scale model of a specific heat exchanger for aero-engines applications in order to relate the effect of the free-stream turbulence to the induced pressure drop through the device. It was reported that a correlation can be found between the mainstream turbulence intensity and the pressure drop mechanism.

Detailed analysis of the flow through a heat exchanger can be carried out using computational fluid mechanics tools. Due to the large demands of grid modeling, this approach requires though very large computer resources and therefore it cannot be part of a large design or analysis package. It is therefore necessary, in the later case, to simulate the correct effect of the heat exchanger on the rest of the system through robust and accurate relationships and methodology.

The aim of the present paper is to develop an industrial tool, which will allow for the accurate representation of the behavior of a heat exchanger within a flow system, i.e., the proper relationship between local velocity and pressure drop. In this way, the system design using computational methods can be carried out without the need for detailed solution of the flow through the passages inside the tube banks. The requirement for the present paper is to develop the correct pressure-velocity relationship, based on experimental data and then, to introduce it in a system and check the validity through comparisons of the detailed velocity distribution with the corresponding experimental ones.

2. The geometry of the heat exchanger and the experimental setup

2.1. The heat exchanger geometry

The heat exchanger operates as a heat recuperator. The aim is to take advantage of the thermal energy of the exhaust gas of the aero-engine. A number of heat exchangers are placed at the exhaust nozzle downstream the turbocompressor. The hot gas passes through the heat exchanger and increases the temperature of the cold ambient air, which circulates inside the tubes. After this stage, the hot (now) ambient air is injected into the combustor. This setup guarantees a high potential of fuel savings and low pollutant emissions. The heat exchanger is formed by U tubes of elliptic cross section arranged in a 4/3/4 staggered configuration. The ends are connected to two cylindrical collectors as shown in Fig. 1a. In this way, the whole tube bank can be considered to consist of a straight part with two matrices and a bow area which is the curved part of the U-shape. The cold air circulates inside the elliptic tubes and the hot gas passes through the characteristic flow passage, shown in Fig. 1b and c, around the elliptic tubes. The distance between the matrices controlled by the radius of the circular section of the U-tubes, called also the "bow region", is limited by manufacturing and mounting considerations inside the exhaust nozzle of the aircraft engine. The side view of the heat exchanger and the geometric details of the staggered arrangement of the characteristic flow passage are shown in Fig. 1b and c. Additional details on the thermomechanical design of the heat exchanger can be found in the work of Schöneborn et al. (2004).

2.2. The experimental setup

To investigate the pressure drop and the flow characteristics of the hot gas side, the 1:1 scale model of the heat exchanger has been constructed. The heat exchanger was placed in a wind-tunnel with a rectangular cross section area equal to $0.346 \times 0.364\,m^2$ as shown in Fig. 2. The hot gas was replaced by ambient air and thus, the heat transfer effects were not examined. In the same figure, the cylinder and the supporting plates used to

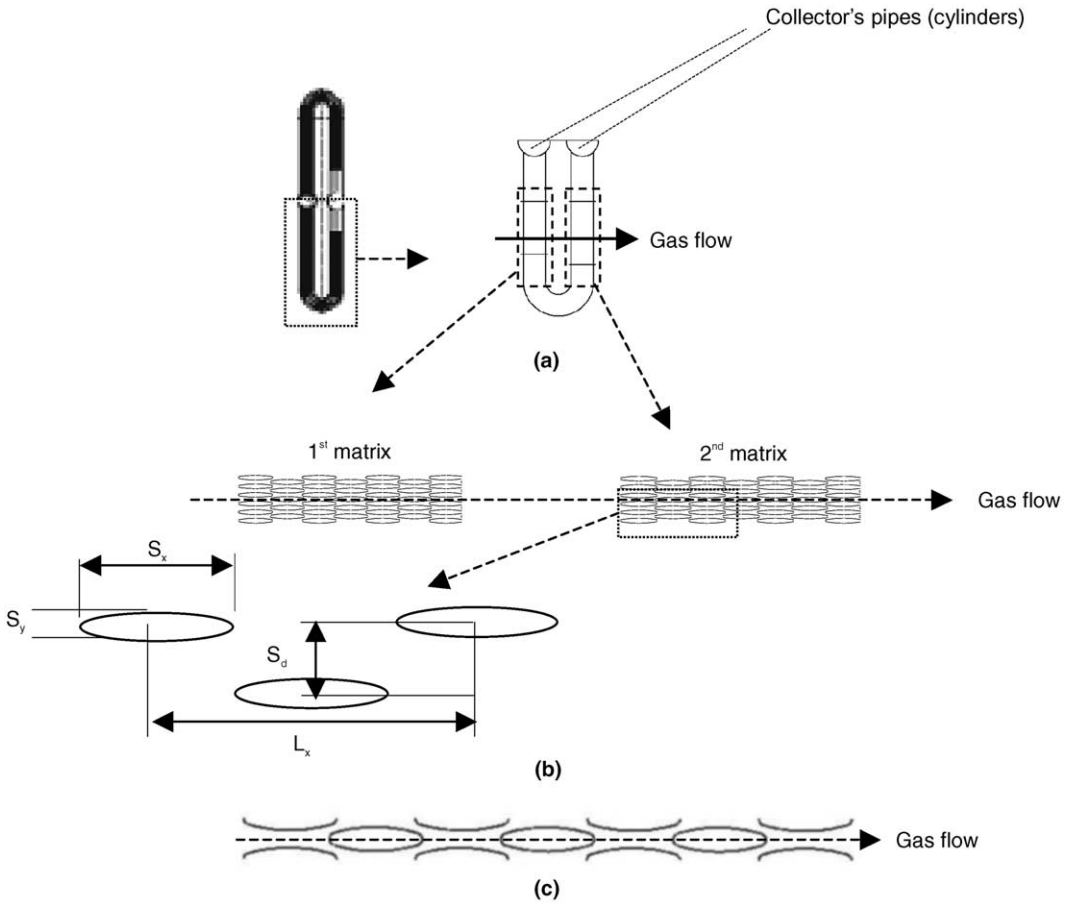

Fig. 1. (a) The heat exchanger's total geometry and the half model used for the experimental measurements and the computational studies, top view, (b) the heat exchanger's matrices with the elliptic tubes in a detailed view showing also the characteristic lengths of the staggered arrangement, side view and (c) the characteristic flow passage for one matrix.

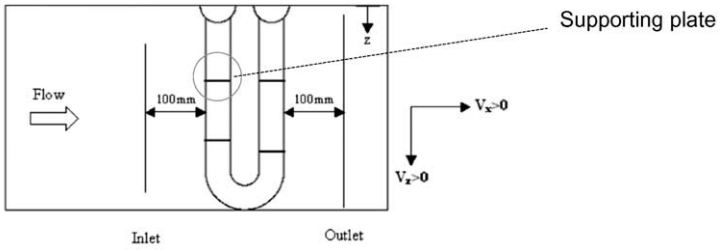

Fig. 2. Geometry of the heat exchanger used—half of heat exchanger's total geometry.

keep the tubes together in a certain distance are illustrated.

Velocity and pressure measurements were carried out at two measurement stations located 100 mm upstream and 100 mm downstream of the model. The experimental measurements that will be presented in this work were performed with the use of a 3-hole pitot-static probe after it has been properly calibrated. The probe consists of three small tubes, one central and two placed in a symmetrical arrangement. Each of these tubes is capable of providing pressure values to a digital manometer attached to the probe. The final signal is transferred to a computer for further processing. The calibration procedure of the 3-hole probe is based on the suggestions of Gundogdu and Carpinlioglu (1998); Morrison et al. (1998) and is described again here in the exact way that it was adapted to the present case.

The 3-hole pitot-static probe pressure values P_1 and P_2 of the side pipes will have equal values only when the tip of the probe is placed parallel to the local airflow direction. For this position, the pressure value of the center pipe P_3 will be equal to the total pressure of the flow at this position. This position is the 0° position of the calibration. Initially, the probe is placed at airflow inside an empty wind-tunnel and by changing the angle with the goniometer the 0° position is found. The P_1, P_2 and P_3 values are recorded. From this position, the orientation of the probe is changed from +30° to −30° (relatively to the 0° position) with a step of 5° and each time the P_1, P_2 and P_3 values are again recorded. At the next stage, the following non-dimensional coefficients are calculated for each angle.

$$C_{\mathrm{p\,yaw}} = (P_1 - P_2)/(P_3 - P_{\mathrm{ave}}), \quad P_{\mathrm{ave}} = 0.5(P_1 + P_2) \tag{1}$$

$$Q_{\mathrm{p}} = (P_3 - P_{\mathrm{ave}})/(0.5\rho V^2) = (P_3 - P_{\mathrm{ave}})/(P_{\mathrm{total}} - P_{\mathrm{static}}) \tag{2}$$

$$S_{\mathrm{p}} = (P_{\mathrm{total}} - P_3)/(P_3 - P_{\mathrm{ave}}) \tag{3}$$

From the measured values and with the use of polynomial curve fitting the functions of the coefficients towards the yaw angle are calculated. In Fig. 3 the plots of the measured dimensionless values are shown together with the polynomial fittings. Through the calibration of the probe used in this work, the R^2 correlation had a value of 0.999. When the probe is placed in a random position inside a flow field in order to derive the total and static pressure, the yaw angle and the velocity components, the reverse procedure is followed. As long as from a specific measurement the P_1, P_2 and P_3 values are known, the $C_{\mathrm{p\,yaw}}$ can be easily calculated. Since from the curve fitting of the $C_{\mathrm{p\,yaw}}$ plot the yaw angle can be derived as a function of the $C_{\mathrm{p\,yaw}}$, by consequence, the flow angle is also known. Furthermore, when the yaw angle is known, the Q_{p} and S_{p} coefficient can be calculated, as well. Finally the values of the velocity, total and static pressure are calculated as:

$$V = \sqrt{\frac{P_3 - P_{\mathrm{ave}}}{0.5\rho Q_{\mathrm{p}}}} \tag{4}$$

$$P_{\mathrm{total}} = S_{\mathrm{p}}(P_3 - P_{\mathrm{ave}}) + P_3 \tag{5}$$

$$P_{\mathrm{static}} = P_{\mathrm{total}} - \frac{1}{2}\rho V^2 \tag{6}$$

An extended literature review, did not give any results for the error estimation of this measurement technique. Nevertheless, one can indicate individually the errors of each measurement device used in the specific technique: The 3-hole probe has an accuracy of 2% referring to the dynamic pressure measurement, which leads to a maximum error of 2 Pa in average. The digital manometer to which the 3-hole probe is connected, has an accuracy of 0.05% giving a maximum error of about 2 Pa. The accuracy of the yaw-angle is estimated at ±1° while the accuracy of the positioning mechanism of the 3-hole probe is estimated at 0.25 mm.

Measurements of total/static pressure and flow angle can provide the velocity magnitude and the two velocity components, which for the present case are the V_x and V_z. During all the measurements, the air density was taken equal to 1.2 kg/m^3 since no temperature variations were observed from the ambient laboratory temperature. Measurements have been carried out for five mass flow rates corresponding to 0.48, 0.91, 1.39, 1.64 and 1.68 kg/s. The measurements covered a wide area of mass flow rates in order to supply adequate results for

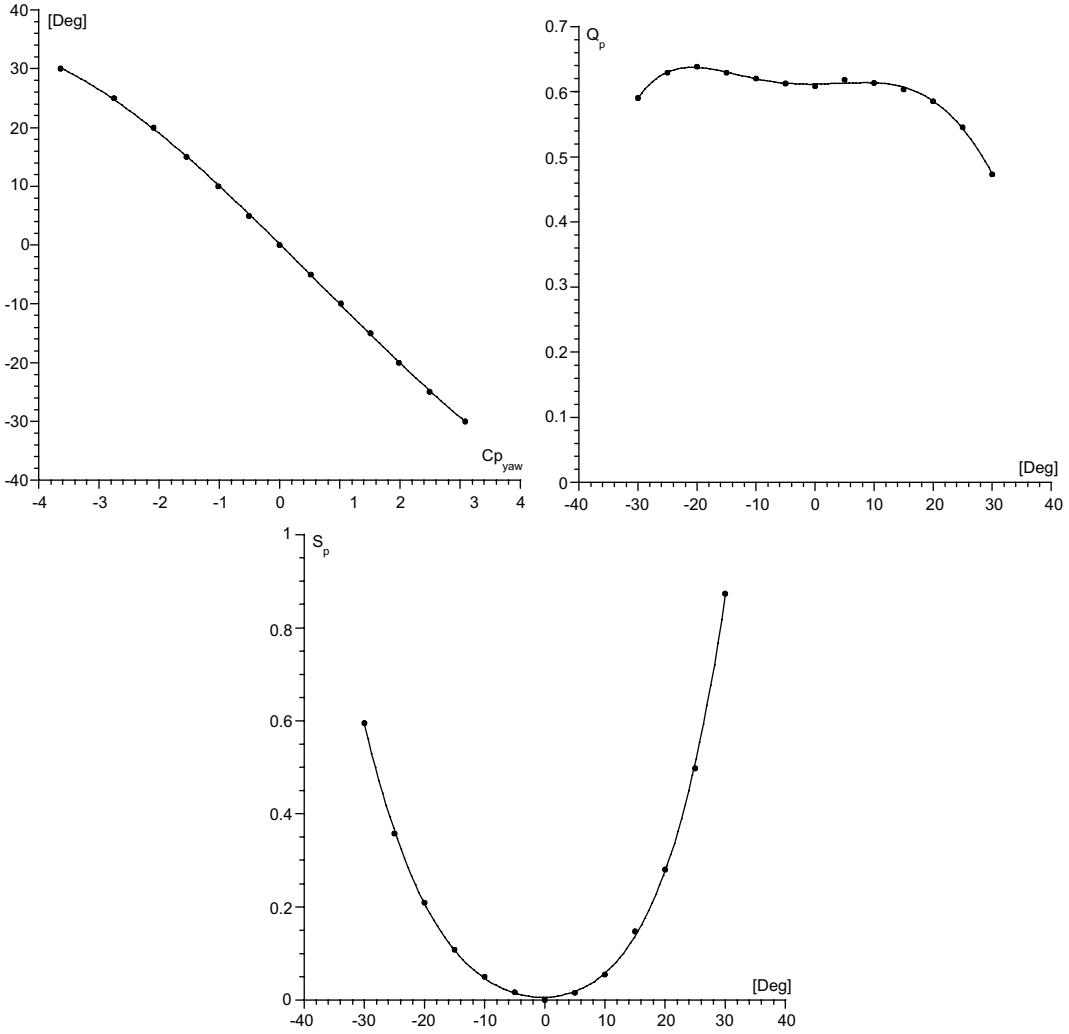

Fig. 3. Plots of the non-dimensionalized coefficients $C_{\mathrm{p\,yaw}}$, Q_{p}, S_{p} towards the flow angle.

the deriving of a static pressure drop law in relation to the effective air velocity through the heat exchanger. Additional measurements were carried out in two planes inside the gap between the two matrices and for two mass flow rates of 0.48 and 1.68 kg/s (corresponding to the minimum and maximum values of mass flow rates), which indicated a pressure recovery inside the gap. The measurement step in the y-direction was chosen to be 10 mm. The zero value for the y-direction corresponds to the symmetry line of the heat exchanger in the vertical direction. This distance has been proved to be sufficient to have a representative picture of the flow development through the heat exchanger and additionally, to obtain realistic average values of the pressure drop. In the z-direction the measurement step was chosen to be 10 mm and 20 mm depending on the local velocity gradient. The z-direction covered the total spanwise distance of the wind-tunnel.

The Reynolds number that characterizes the flow through the characteristic passage is defined as follows:

$$Re = \frac{V_{\max} \cdot d}{\nu} \tag{7}$$

where $V_{\max}$ is the average maximum velocity obtained in the minimum gap between the tubes in all directions (Fig. 1b). In the literature there is a variety of suggestions for the choice of the characteristic length, d. This length can be either the thickness of the elliptic tubes (minor diameter of the ellipse), the chord length of the elliptic tubes (major diameter of the ellipse) or the minimum gap between the tubes. In order to investigate the nature of the flow (laminar, transitional of turbulent) the suggestions of Umeda et al. (1999) were adopted. Thus, d was chosen to be equal to the minimum diameter of the ellipse. Since it was not possible to measure the velocity inside the minimum gap due to the space limitations (where one expects to have the maximum velocity values), the value $V_{\max}$ was estimated by applying the continuity equation in a characteristic passage for the five examined mass rates. After these approximations, $V_{\max}$ was calculated to have a range of values from 3.2

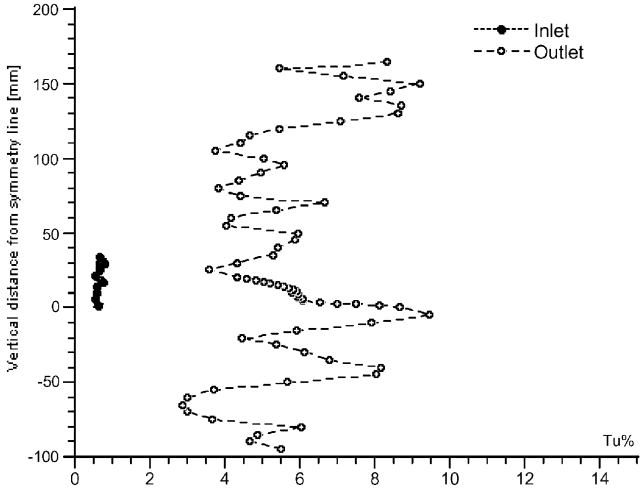

Fig. 4. Turbulence intensity level.

to 10.9 m/s and the corresponding Reynolds numbers in a range from 794 to 2708. As already reported by Umeda et al. (1999), for flow over tube bundles, the laminar flow regime is observed for $Re < 200$ while the turbulent one for $Re > 6000$. Consequently, the Reynolds numbers of the experimental measurements lie in a range that characterizes the flow through the heat exchanger as transitional and for the smaller mass flow rates are very close to laminar. This observation will be exploited in the CFD modeling.

In order to investigate the turbulence levels at the inlet and at the outlet of the test section (inlet and outlet regions of the heat exchanger), additional velocity measurements have been carried out using the Hot Wire Anemometry technique for the maximum inlet mass flow rate. Fig. 4 shows the percentage of the turbulence intensity levels. From these diagrams, it can be shown that the turbulence intensity has low values at both regions with average values 0.6% and 5.8% respectively. For the region located at the exit of the test section, variations of the turbulence intensity are observed which are related to the wake formation behind the heat exchanger tubes.

3. Pressure drop measurements

In order to derive the relationship between the static pressure drop and the mass flow through the heat exchanger, the measured pressure difference and an effective velocity were considered. The typical pressure difference for the present case is the one *in the straight part* of the matrix, contained between two supporting plates, as it is away from any boundaries or other external effects. For this part, the flow encounters only the characteristic passage of the elliptic tubes, shown in Fig. 1. The measured values of the pressure and velocity flow parameters in this area were used for both the inlet and the outlet planes.

3.1. Calculation of the effective mean axial velocity based on the experimental data

For each inlet mass flow rate the mean axial V_x velocity component was calculated. Additionally, using the experimental data, the average values of the static pressure drop between the inlet and the outlet planes for each inlet mass flow rates were also obtained. An effective inlet velocity right before the heat exchanger's inlet was introduced. Its value was calculated at station 2 (Fig. 5) based on a simple application of the continuity equation.

Additionally, and since the gap inside the heat exchanger is not modeled as part of the porous block it is important to find the pressure drop attributed to each matrix. As the pressure drop through the heat exchanger is measured at the straight part, it was assumed that half of the pressure drop is occurring as result of the existence of the first matrix and the remaining half is due to the second one. Based on the above measurements and assumptions, a relationship between the pressure drop in each matrix as a function of the effective velocity can be derived.

3.2. Derivation of the pressure loss model

In Table 1, the values of the streamwise effective velocity $V_{x-\text{effective}}$ and the static pressure drop *for the straight part* of one matrix are presented. From the last two columns a pressure drop law was derived as shown in Fig. 6.

In order to investigate the pressure drop behavior of the heat exchanger, a direct comparison has been performed with the pressure drop laws reported by Kays and London (1984). For the closest heat exchanger configuration, which is the one with staggered finned flat tubes, the pressure losses are expressed through the friction factor f which is a function of the static pressure drop between the inlet and the outlet side of the heat exchanger, the mass flow through the heat exchanger, the

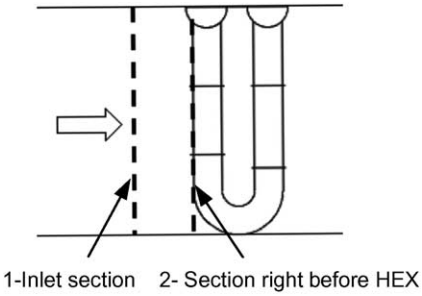

Fig. 5. Sections used for the calculation of the effective velocity.

Table 1
Values used for the pressure drop law

kg/s	DPstatic [Pa]	$V_{x-\text{mean}}$ [m/s]	Axial velocity correction factor	$V_{x-\text{effective}}$ V_{eff} [m/s]	50% of DPstatic [Pa]
0	0.0	0.00	1.1019	0.00	0.0
0.48	249.8	3.18	1.1019	3.50	124.9
0.91	769.9	6.01	1.1019	6.62	384.9
1.39	1673.8	9.23	1.1019	10.17	836.9
1.64	2303.3	10.85	1.1019	11.96	1151.6

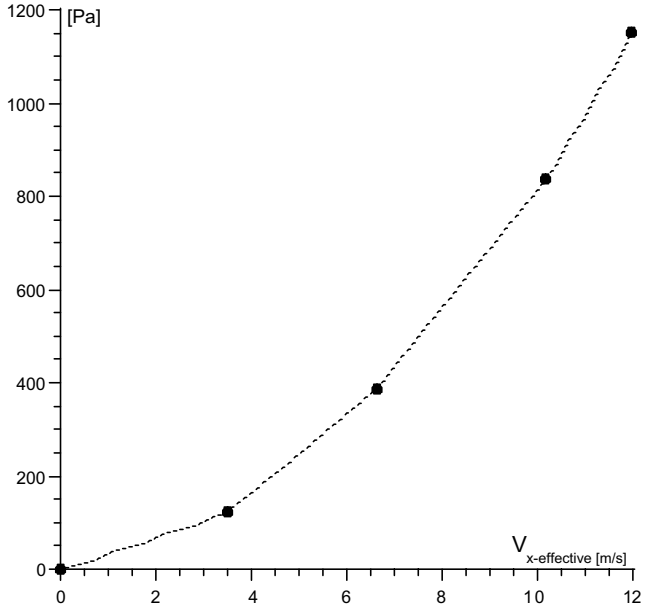

Fig. 6. Static pressure drop of the straight part of the heat exchanger.

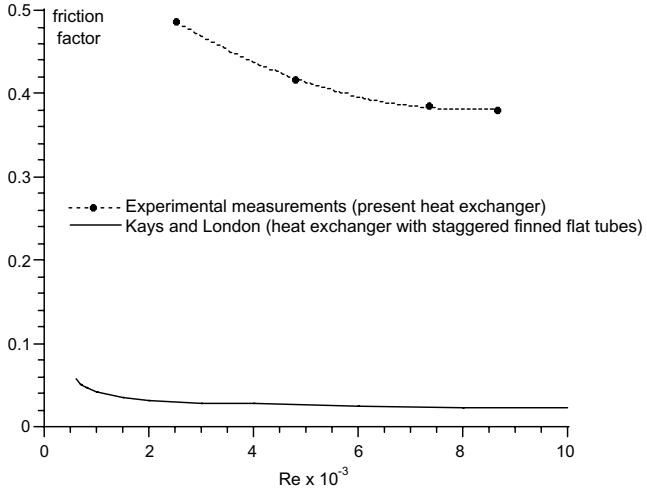

Fig. 7. Comparison of friction factors between the present heat exchanger and a heat exchanger with a close configuration.

porosity and the geometry of the heat exchanger. The friction factor f is calculated in its general form as:

$$f = \left[\frac{r_h \cdot v_{inlet}}{L \cdot v_m}\right] \cdot \left[\frac{2\Delta P \cdot g}{G^2 v_{inlet}} + (1+p^2)\left(1 - \frac{v_{outlet}}{v_m}\right)\right] \quad (8)$$

$$G = \frac{m}{pA_{fr}} \quad (9)$$

where A, heat exchanger total heat transfer area; A_{fr}, heat exchanger total frontal area; ΔP, static pressure drop; g, proportionality factor in Newton's second law; L, flow length of the heat exchanger tubes; p, average porosity of the matrix surface, dimensionless; ρ_{inlet}, the average density of air at the inlet side of the heat exchanger; ρ_{outlet}, the average density of air at the outlet side of the heat exchanger; r_h, hydraulic radius of the heat exchanger (equal to $\frac{pA_{fr}L}{A}$ for heat exchanger matrix surfaces); v_{inlet}, specific volume at the inlet side of the heat exchanger (equal to $\frac{1}{\rho_{inlet}}$); v_{inlet}, specific volume at the outlet side of the heat exchanger (equal to $\frac{1}{\rho_{outlet}}$); v_m, mean specific volume (equal to $\frac{v_{inlet}+v_{outlet}}{2}$).

The average Reynolds number of the flow field in the heat exchanger presented in Fig. 7, is calculated as:

$$Re = \frac{4r_h G}{\mu} \quad (10)$$

where μ is the dynamic viscosity.

For the estimation of the porosity, a characteristic flow path inside the straight part area (Fig. 1c) of the heat exchanger under investigation was used as being the most suitable to provide the most representative properties of the heat exchanger. The average porosity of the heat exchanger was calculated as the ratio of the free passage area of the flow inside this passage to the total area that the geometry of the heat exchanger occupies from the leading edge of the first elliptic tube to the trailing edge of the last elliptic tube of one matrix of the heat exchanger. In order to calculate the free passage area of the flow, from the total area of the passage, the area occupied by the elliptic tubes was subtracted. The remaining part was the available free flow area inside the heat exchanger.

For the estimation of the specific volumes it should be noted that the flow is almost totally incompressible with the average density of the air in the inlet and the outlet side of the heat exchanger being constant and equal to $1.2\,\text{kg/m}^3$.

Fig. 7 shows the comparison between the two friction factors. It can be shown that in both cases, the same tendency is met.

In order to proceed to a numerical simulation there is a need for a mathematical relationship that will be extracted using polynomial curve fitting approximating the experimental data. Two relationships have been considered. The first one is an elliptic equation of the following form:

$$\Delta P = aV_{\text{eff}}^{n} \tag{11}$$

while the second is a parabolic equation of the form:

$$\Delta P = aV^2 + bV \tag{12}$$

For both equations, the values of b and n are calculated through the curve fitting procedure. The corresponding pressure drop laws for the present case take the following forms (having always a mean square root error less than 0.1%):

$$\text{Model 1} \quad \Delta P_{\text{st,exp}} = 10.245 V_{\text{eff}}^{1.906} \ [\text{Pa}] \tag{13}$$

$$\text{Model 2} \quad \Delta P_{\text{st,exp}} = 7.171 V_{\text{eff}}^{2} + 10.088 V_{\text{eff}} \ [\text{Pa}] \tag{14}$$

These two models were used to simulate the effect of the heat exchanger package in the wind-tunnel in order to define the best type of model to be used.

4. Porous medium simulation of the heat exchanger geometry

4.1. General implementation

The heat exchanger consists of a large number of pipes with an elliptic profile. For the computational purposes one would need to construct a very detailed grid outside and inside the numerous characteristic flow passages that form the heat exchanger. By consequence the need for computer CPU and memory requirements would be enormous. So, if one needs to study computationally the flow field in a large system, this makes the computational task impossible. However, it is possible to model the heat exchanger's matrices by approximating them as being *isotropic* porous media with a prescribed pressure drop as a function of the local velocity. The local velocity is in general three-dimensional. In the present case, the mean velocity angle of attack for each symmetric-elliptic tube is zero and thus, the only force acting, due to an imposed pressure difference, is the one in the streamwise direction. Consequently, the main contributor to the pressure drop terms is the streamwise velocity component. The advantage of this action is that there is no need to model all the characteristic passages but the restriction is located to the need of having a realistic and representative pressure drop law through the heat exchanger. This method can provide a good and not computationally expensive solution of the flow field especially when the interest is not so much focused to the flow in the direct vicinity of the heat exchanger (where one would expect the modeling of the wakes induced by the elliptic tubes), a case which is not too uncommon in related industrial applications.

The flow field inside the wind-tunnel and through the heat exchanger is modeled with the use of FINE™ integrated package of NUMECA International. The heat exchanger is modeled by a number of porous media with a prescribed pressure drop law for each of them. In the upstream and the downstream region of the heat exchanger typical structured grids are constructed. The same holds also for the region between the two matrices. The number of porous media and the way that the porous media blocks are used to cover the heat exchanger geometry depends on the adopted pressure drop model due to some limitations imposed by the commercial CFD package. In the present methodology, a maximum of fifteen blocks can be used, provided that the model 1 is used for the pressure drop velocity relationship. If a second order polynomial is used, the number of blocks is reduced to seven only. This means that there is a compromise to be made between the accuracy of the geometry representation and the accuracy of the pressure drop law. In this paper both approaches have been used which differ both in the porous blocks subdivision of the heat exchanger and the function of pressure drop law applied.

The computational domain used for the heat exchanger was subdivided into a number of porous blocks using two approaches. The first approach, Fig. 8a, corresponding to the equation of model 1 consists on the subdivision using 14 blocks for the porous media and the second approach, Fig. 8b, consists of 7 blocks, for the porous media. The computational domain outside the heat exchanger area was the same for the two models. In both cases, the two cylindrical manifolds (collector pipes) and the supporting plates were also modeled, as this has been proved necessary in order to obtain a good solution of the flow field in the wake region behind the heat exchanger.

The gap between the two matrices of the heat exchanger is not part of the porous medium, as in this region the pressure recovery is expected. The bow region was subdivided in the way shown in Fig. 9 where the limits of each block in this region are plotted. As it can be seen, the porous medium blocks start from the leading edge of a tube and end at its trailing edge. Only for the last tube, two porous blocks were used in order to improve the resolution of the flow field near the wind-tunnel sidewall as shown in the detailed view of Fig. 8a. The division of the bow region into eight porous medium blocks creates domains with different porosities as the ratio of total area to the free passage area changes along the geometry subdivision.

When the second model is used, Fig. 10, seven porous medium blocks were used. For the bow region only three

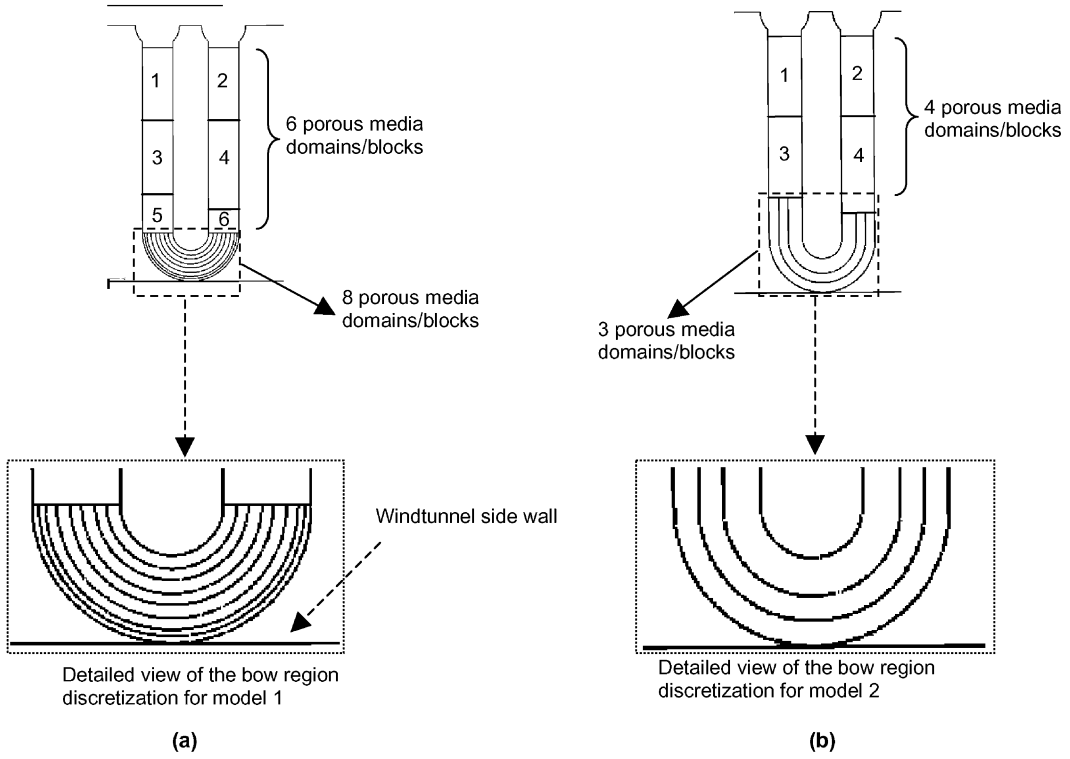

Fig. 8. Heat exchanger subdivision into porous medium blocks. (a) Model 1 and (b) Model 2.

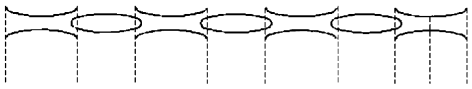

Fig. 9. Discretization of bow region into separate porous medium domains—Model 1.

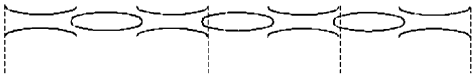

Fig. 10. Discretization of bow region into separate porous medium domains—Model 2.

porous medium blocks were used for the modeling. The discretization of the bow region was not as detailed as in the first model but the pressure drop applied was approximated better using the second order polynomial form.

The two forms of the pressure drop given by Eqs. (13) and (14) are introduced to the flow solver in order to estimate which model performs better. The pressure drop law is added as an additional source term in the discretized momentum equations. No additional modification is made to the turbulence model equations. The results of the CFD approach have been compared with the experimental measurements both for the velocity and pressure distributions. For evaluation purposes, at the final stage the average absolute error in Pascals and the percentage error were compared.

5. Modeling of the flow field

In the computational modeling, the flow field through the heat exchanger was treated as steady and two-dimensional. At first, it was important to compare the results of the two porous models in a relatively medium size grid in order to get an indication of the quality of the applied pressure drop law. The solutions were validated with the averaged experimental values and the better model was chosen to be the one with the lower average error percentage of the static pressure drop. In the next step, a finer grid was used to investigate the grid dependency on the solution and to check whether the formerly computed results were reliable. As it will be shown later, whilst these grids were not fine enough for full grid-independence studies, the overall pressure drop was adequately captured on them.

As already mentioned, the computational domain covers the wind-tunnel setup with the heat exchanger model placed inside it. The grid constructed in the computational domain upstream and downstream the heat exchanger region was exactly the same (by means of the number of nodes and of the quality) for the two models. However, the grid used for the discretization of the heat exchanger (and thus for the adoption of

the pressure drop model) was different due to the difference in the bow region porous media blocks. The CFD approach was based on the solution of the discretized Navier–Stokes equations using the control volume technique. The discretization scheme was the central one with a second order accuracy. Details on the solution approach can be found in the manuals of FINE™ (2001) commercial CFD package. At the inlet section of the computational domain, total conditions were imposed, i.e. the total pressure and the total temperature of the flow. These were equal to the experimental ones. At the outlet, the mass flow (and thus the velocity) was corrected by adopting the condition of overall mass continuity. The values of the pressure at the outlet were computed by using a linear extrapolation from the internal grid points. The major problem within this study was the choice of using or not a turbulence modeling of the flow. As already mentioned above, the Reynolds numbers corresponding to the four inlet mass flow rates, range from values close to the laminar regime of the flow (794) to values inside the transitional regime of the flow (2908). Thus, two model approaches have been performed using one final chosen grid, after grid dependency studies and by assuming the flow to be either laminar of turbulent. The computational results have been compared with the experimental data. For the turbulent flow modeling, the k-model in its low-Reynolds formulation after Launder and Sharma has been adopted. The reason for this choice was based on the remarks of Savill (2002) which indicated that generally and for transitional industrial flows this model gives satisfactory results for the velocity distributions. The inlet values for the turbulent kinetic k were set after detailed experimental measurements upstream the model heat exchanger. For the inlet, the longitudinal turbulence intensity T_u had an averaged value of 0.6%, obtained from the hot-wire anemometry measurements. This value was used in the cases of the turbulent flow modeling by using the indicative semi-empirical equation that related the turbulent kinetic energy with the turbulence intensity:

$$k = \frac{3}{2}(V_{\text{eff}} T_u)^2 \tag{15}$$

while for the turbulence dissipation rate a characteristic turbulent length scale l was used in order to describe the values of this parameter at inlet using the equation:

$$\varepsilon = \frac{c_\mu^{3/4} k^{3/2}}{l} \tag{16}$$

where $c_\mu = 0.09$. For the present case, l was chosen to take a value equal to the collector's cylinder radius because it is considered that the wake structures formed behind this entity give an indication of the possible largest eddy through the flow field. Although it is well known that the choice of this parameter can affect the quality of the velocity distributions and especially of the turbulent quantities distributions, it was assumed that the choice can not affect the general solution since the primary interest of this study is focused on the general industrial approach of the flow development. Special attention was given for the near wall grid points in order to have the local y^+ values lower than 1 since a low-Reynolds model was adopted. Convergence occurred after about 12 h minimum or 24 h maximum at an Intel Pentium 4 1.5 GHz (real user time, depending on the grid size) with a convergence criterion less or equal to 10^{-5} for the averaged residuals of the computed flow variables.

5.1. The grid used for the two pressure drop models

For the model 1, a grid of 55,000 points approximately was used. Thirty-one independent blocks were used to cover the geometry in detail of which fourteen were characterized as porous domains. For the model 2 a grid of 48000 points approximately was used. Twenty-four independent blocks were used to cover the geometry in details of which seven were characterized as porous domains. The difference in the number of grid points is due to the different topology that each model introduces in the grid construction. Generally, this difference is not very important as long the excess points of model 1 were given to cover better the connection areas of the porous blocks in the bow region so as to avoid inconsistencies in those areas during the solution convergence. In model 2, since only three porous blocks were used in the bow region, a smaller number of grid points was adequate to ensure the convergence of the solution. Furthermore, as the supporting plates were also modeled, it was necessary to add grid points to create a finer computational domain embracing the plates and the area right downstream where a wake formation is expected to appear. The gap inside the heat exchanger's matrices was modeled with a combination of H-type and C-type grids in order to model in a better way the bow region area. Pictures of the computational grid in various regions are listed in Figs. 11–13. The darker areas represent areas where the grid was finer locally in order to provide better resolution of the flow field. As it can be seen in Figs. 12 and 13 the denser parts are the parts near the wind-tunnel side walls where the need to solve in detail the flow field in the wake of the cylinders and the need to investigate the effect of the bow region were met. The straight part was covered with a coarser grid due to the relative simplicity of its geometry.

5.2. Validation and adoption of the pressure drop model

In order to check only the quality of the two porosity models the first comparisons were performed by assuming that the flow is in the *laminar* regime. The flow field was computed for four mass flow rates corresponding to 0.48, 0.91, 1.39 and 1.68 kg/s. The computational results

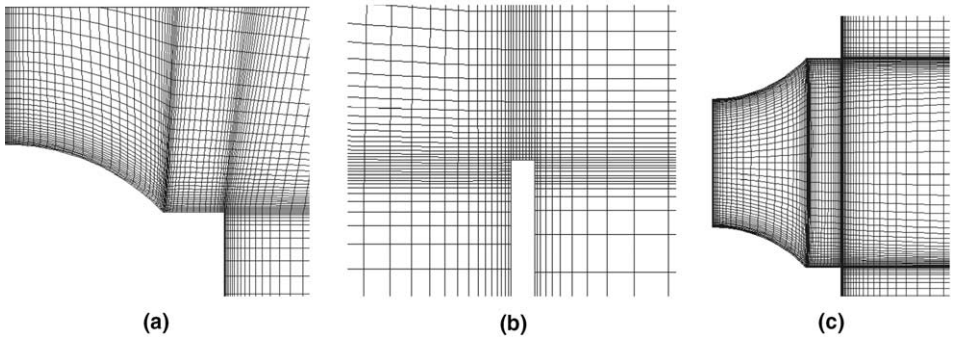

Fig. 11. (a) Details of the grid near the collector's cylinder, (b) around the supporting plates and (c) at the gap between the two matrices and near the collector cylinders.

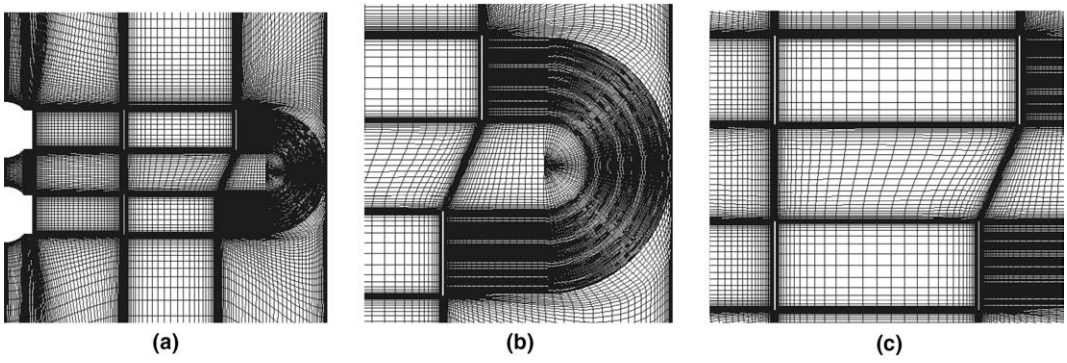

Fig. 12. Model 1: (a) computational grid around the heat exchanger, (b) grid at bow region and (c) grid at the straight part.

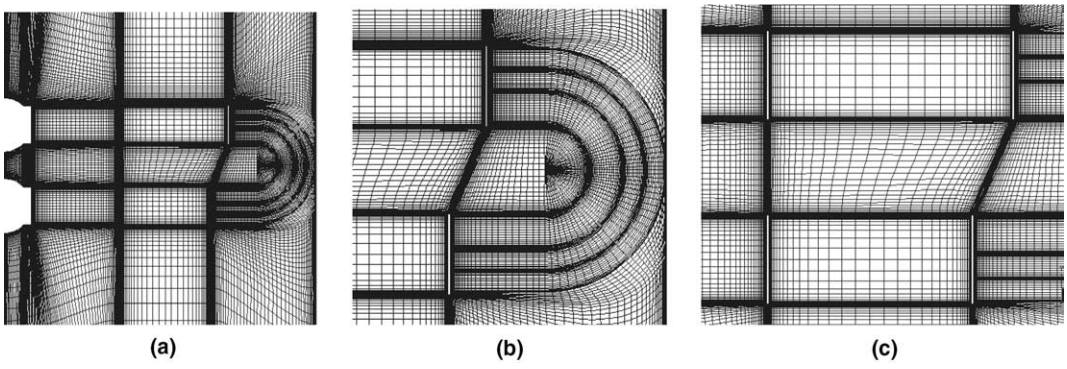

Fig. 13. Model 2: (a) computational grid around the heat exchanger, (b) grid at bow region and (c) grid at straight part.

were compared to the measured values of the flow parameters at the inlet and outlet sections. The values of the total and static pressure, axial V_x velocity and spanwise V_z velocity are plotted in the diagrams of Figs. 14 and 15 for the minimum and maximum inlet mass flow rate. Additionally, the pressure drop between the inlet and outlet levels and for the middle of the distance between the supporting plates was compared with the one obtained by the calculations. The comparisons for the four inlet mass flow rates are presented in Tables 2 and 3.

Generally, there is a good agreement between experimental and computational results. The total and static pressure drop error is in an acceptable range for both models apart from the small values of mass flow rate for model 1 where an increased error is computed. For model 1 the pressure drop error percentage ranges from 0.41% to 13.4% where for model 2 the error percentage ranges between 1.5% and 4.4%. Since no major differences exist between the velocity profiles of models 1 and model 2 the resultant difference in the pressure drop error percentage leads to the conclusion that the more

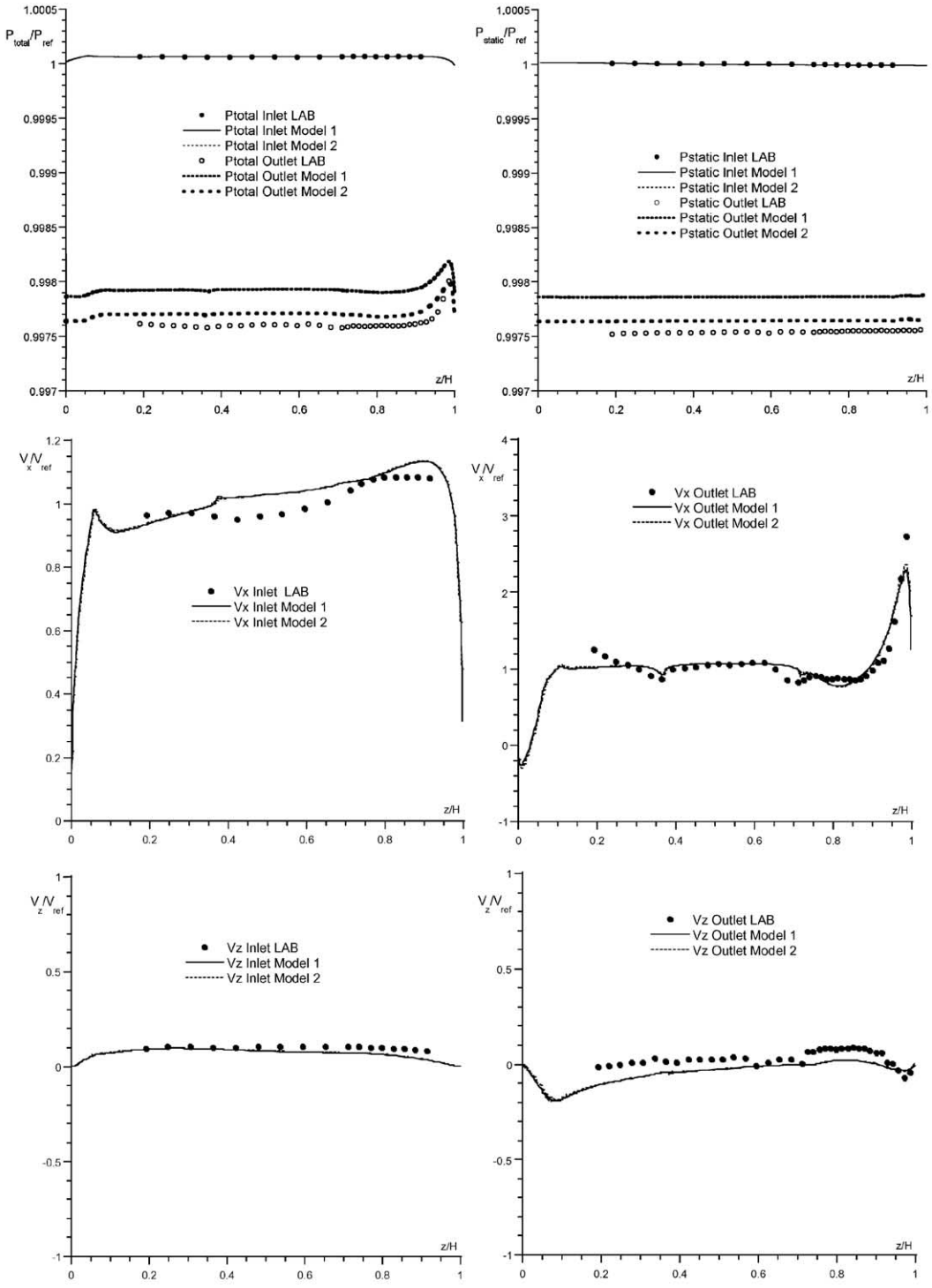

Fig. 14. Static/total pressure and velocity components for the minimum inlet mass flow. Comparisons with the measurements.

detailed discretization of the bow region of model 1 made no difference to the predictions of the flow field development. On the other hand the use of a second order polynomial pressure drop law in model 2 instead of a hyperbolic one like in model 1 gave more reliable results as the error was computed to be always under 4.4%. By calculating the average error of models 1 and 2 it is shown that model 2 is better by 2% approximately.

5.3. Grid dependency studies

After the final adoption of porous model 2, alternative grids were tested in order to conclude to a certain

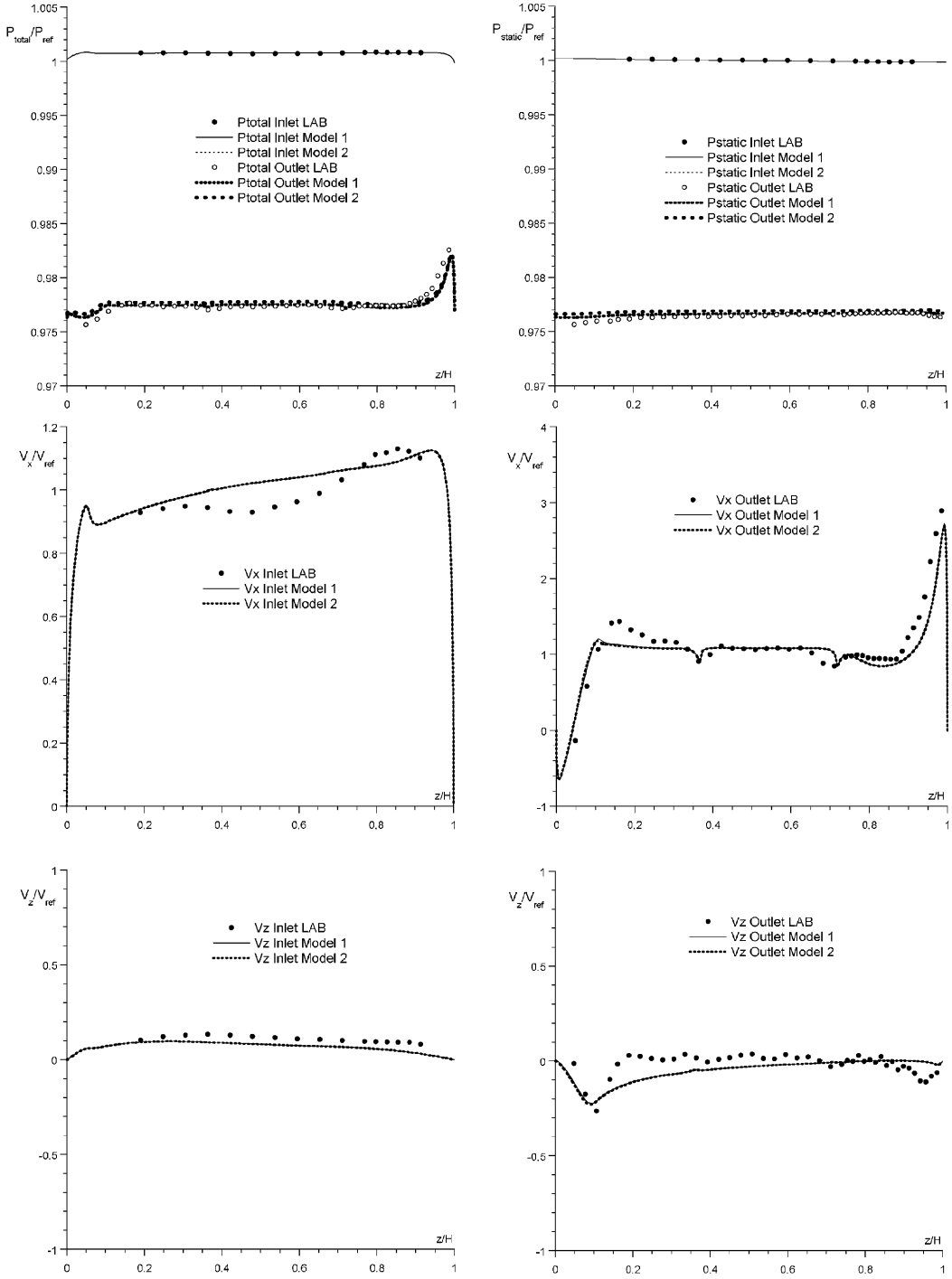

Fig. 15. Static/total pressure and velocity components for the maximum inlet mass flow. Comparisons with the measurements.

Table 2
Pressure drop error of porous model 1

Mass flow rate (kg/s)	Abs(ΔP_{total} error%)	Abs(ΔP_{static} error%)
0.48	13.23	13.38
0.91	5.70	5.90
1.39	1.05	1.27
1.68	0.40	0.95
Average value	5.09	5.38

Table 3
Pressure drop error of porous model 2

Mass flow rate (kg/s)	Abs(ΔP_{total} error%)	Abs(ΔP_{static} error%)
0.48	4.26	4.41
0.91	4.20	4.42
1.39	1.85	2.05
1.68	1.55	2.08
Average value	2.97	3.24

set of grid dimensions for having grid independency. Three grids having the same quality and different number of nodes were used. The basic grid was chosen to be the one used for the accuracy tests of the two porous models, named as grid 1. Grid 2 was a similar grid having a double density for the nodes in the z-direction while grid 3 had a double density for the nodes in the x-direction. The test of a full-double dimension grid was found to be impossible for application due to the large amounts of memory and CPU requirements. The grid independency studies were performed for both laminar and turbulent cases. Table 4 summarizes the information for the grids used in the present study while Tables 5 and 6 present comparative results of the error percentage between the various cases that were examined. As it can be seen the error difference between the various solutions is 0.25% approximately, a difference which is less than 3 Pa. Thus, it can be stated that *for the pressure drop* all of the solutions provide grid independent results.

Finally, it was found that the basic grid 1 could not capture in a satisfactory way the wake behind the collector's cylinders and the supporting plates. Grid 3 gave the best results in preliminary computational tests for both laminar and turbulent cases with a lesser number of nodes.

Table 4
Grid dimensions and convergence real user time

	Number of nodes	Information	Convergence real time [h]
Grid 1	49108	Basic grid	~12
Grid 2	97338	Denser in z-direction	~24
Grid 3	96554	Denser in x-direction	~24

5.4. Comparison between laminar and turbulent flow modeling

Since the flow is located in the transitional regime and in order to investigate whether a turbulent or a laminar flow modeling gives results that are closer to the real flow, comparative studies of the two approaches have been performed. In Fig. 16, the vector plots of the two approaches are shown together with the contour plots of the static pressure. The plots refer to the maximum inlet mass flow and they are presented in order to have an integrated picture of the flow development through the heat exchanger. Similar plots have been obtained for the other cases corresponding to the various inlet mass flows. All the results that will be presented hereafter are referring to computations performed using the final chosen grid number 3.

Generally, no major differences appear between the laminar and the turbulent approach. With a careful observation, the only difference is this one concerning the development of the wake behind the collector's pipe (corresponding to plot c in the Fig. 16). The turbulent approach predicts a smaller wake region. In the comparative velocity components diagrams this difference will be shown in a clearer way. Additionally, on the same figures, the flow region behind the supporting plates is shown, where two attached vortices are forming, giving a typical wake distribution in the velocity profiles.

In Figs. 17 and 18 the comparative diagrams of the flow quantities with both laminar and turbulent solutions and for the minimum and maximum inlet mass flows are shown. Concerning the comparative diagrams the velocity values are non-dimensionalized by the reference velocity which is the velocity corresponding to the inlet mass flow, while the pressure values (either total or static) are non-dimensionalized by the reference static

Table 5
Total pressure drop absolute error percentage for the various grids examined

kg/s	Grid 1-laminar	Grid 2-laminar	Grid 3-laminar	Grid 2-turbulent	Grid 3-turbulent
0.48	4.26	4.14	4.06	4.10	3.98
0.91	4.20	4.10	4.02	4.01	4.00
1.39	1.85	1.72	1.66	1.65	1.61
1.68	1.55	1.44	1.35	1.39	1.31
Average value	2.97	2.85	2.77	2.79	2.72

Table 6
Static pressure drop absolute error percentage for the various grids examined

kg/s	Grid 1-laminar	Grid 2-laminar	Grid 3-laminar	Grid 2-turbulent	Grid 3-turbulent
0.48	4.41	4.37	4.21	4.33	4.13
0.91	4.42	4.33	4.20	4.28	4.20
1.39	2.05	1.90	1.85	1.88	1.81
1.68	2.08	1.95	1.87	1.95	1.86
Average value	3.24	3.14	3.03	3.11	3.00

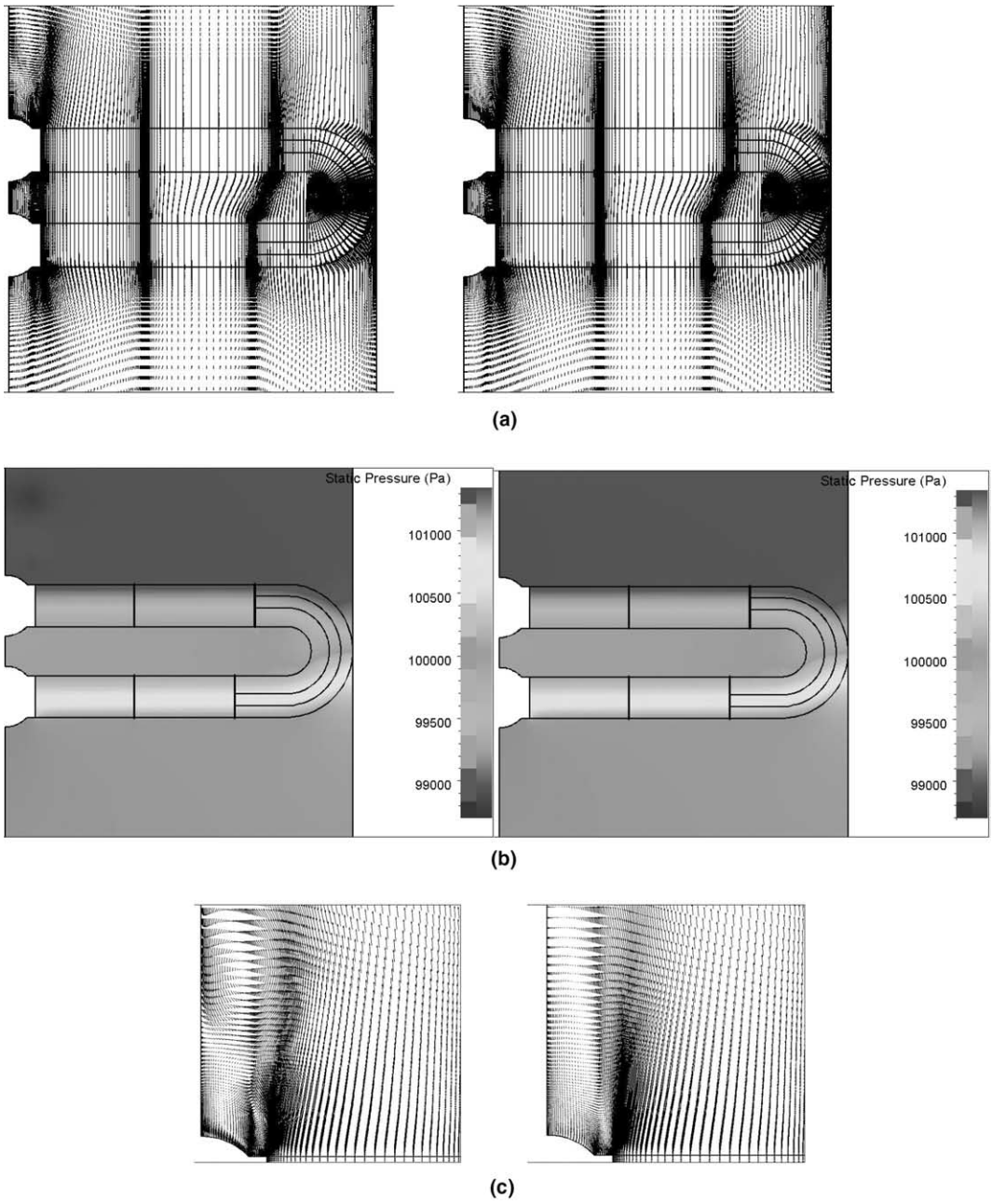

Fig. 16. Maximum inlet mass flow, laminar (left) and turbulent (right) solution: (a) Vector plot through the heat exchanger, (b) contour plot of static pressure, (c) detailed vector plot in the region behind the collector's cylinder, (d) detailed vector plot in the region behind the supporting plate and (e) vector plot at the outlet region of a characteristic flow passage.

pressure measured at the inlet. The distances on the x-axis of the diagrams are non-dimensionalized by the wind-tunnel's spanwise distance H. It should be noted here that the low values of the dimensionless spanwise distance refer to the region close to the collector's cylinder (left part of the diagrams).

Concerning the values of the total and static pressure, it can be concluded that no major differences appear between the laminar and turbulent approach for the two inlet mass flows. Thus, for this range of Reynolds numbers, both the approaches give satisfactory results when a two dimensional modeling is performed. However, this is not the case for the velocity profiles at the outlet region. A close examination of the above figures shows that the laminar solution is in a better agreement with the experimental measurements than the turbulent solution. This is more clearly shown in the region behind the cylinder where a large wake is formed by means of a separated flow region (lower values of z/H on the x-axis). The laminar solution predicts an axial velocity, which

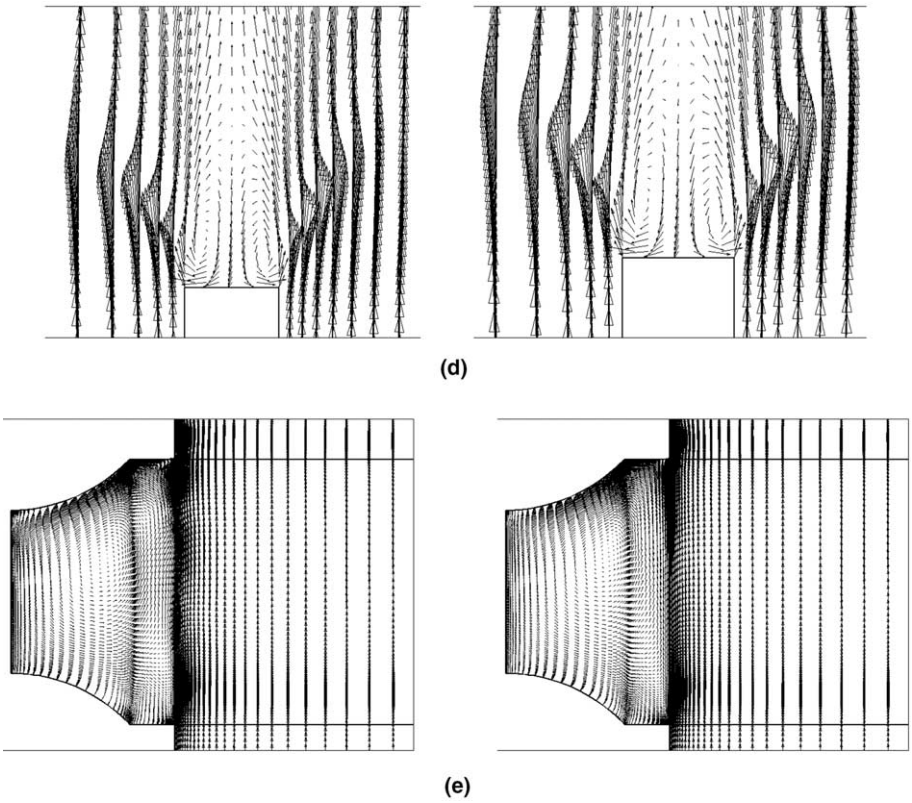

Fig. 16 (*continued*)

has the same trend with the experiments while this does not occur for the turbulent case. For the turbulent case the recirculation region is significantly underpredicted. Consequently, the computed shear layer region in the separated zone is smaller for the turbulent case. Thus, the local increase of the axial velocity in this region is underpredicted. For the laminar cases, the wake region is correctly predicted leading to a more realistic velocity field representation. The comparisons for the spanwise velocity components have also the same qualitative behavior. The laminar solution behaves better towards the experimental measurements. A lower spanwise velocity is computed in the laminar case as the result of a prediction of a larger recirculation region compared to the turbulent solution. The fact that the laminar solution provides better results is a possible indication that the flow in the cases examined lies in the transitional regime and more closely to the laminar than the turbulent one.

6. Conclusions

A specific type of a heat exchanger for aero-engine applications has been examined by means of experimental measurements and computational modeling. The investigation has been focused on the flow development through the heat exchanger, thus only the flow quantities and not the heat transfer mechanisms have been examined. The characteristic Reynolds numbers governing the flow were calculated to be in the range of the transitional range for all of the examined cases by means of a variable inlet mass flow. Velocity and pressure measurements have been carried out at the inlet and outlet sections of the device in order to derive the pressure drop through it and the velocity distributions downstream the heat exchanger. For the measurements, a 3-hole pitot-static tube was used after proper calibration.

The main varying parameter was the inlet mass flow and in relation with it, a pressure drop law was derived in order to adopt it into a computational modeling procedure. The pressure drop law was derived from a *straight part* of the heat exchanger, i.e. from a small region where no curved tubes exist. This pressure drop law was applied later in the computational procedure to the total heat exchanger package, *including straight and curved parts*. In the computational procedure, the heat exchanger was modeled by several porous medium blocks since its complicated geometry made impossible the generation of an affordable (for a typical personal computer) grid. Two porous medium laws were tested and the one having a second order accuracy was finally selected after a back to back comparison on a medium size grid having 49,108 computational nodes. Additionally,

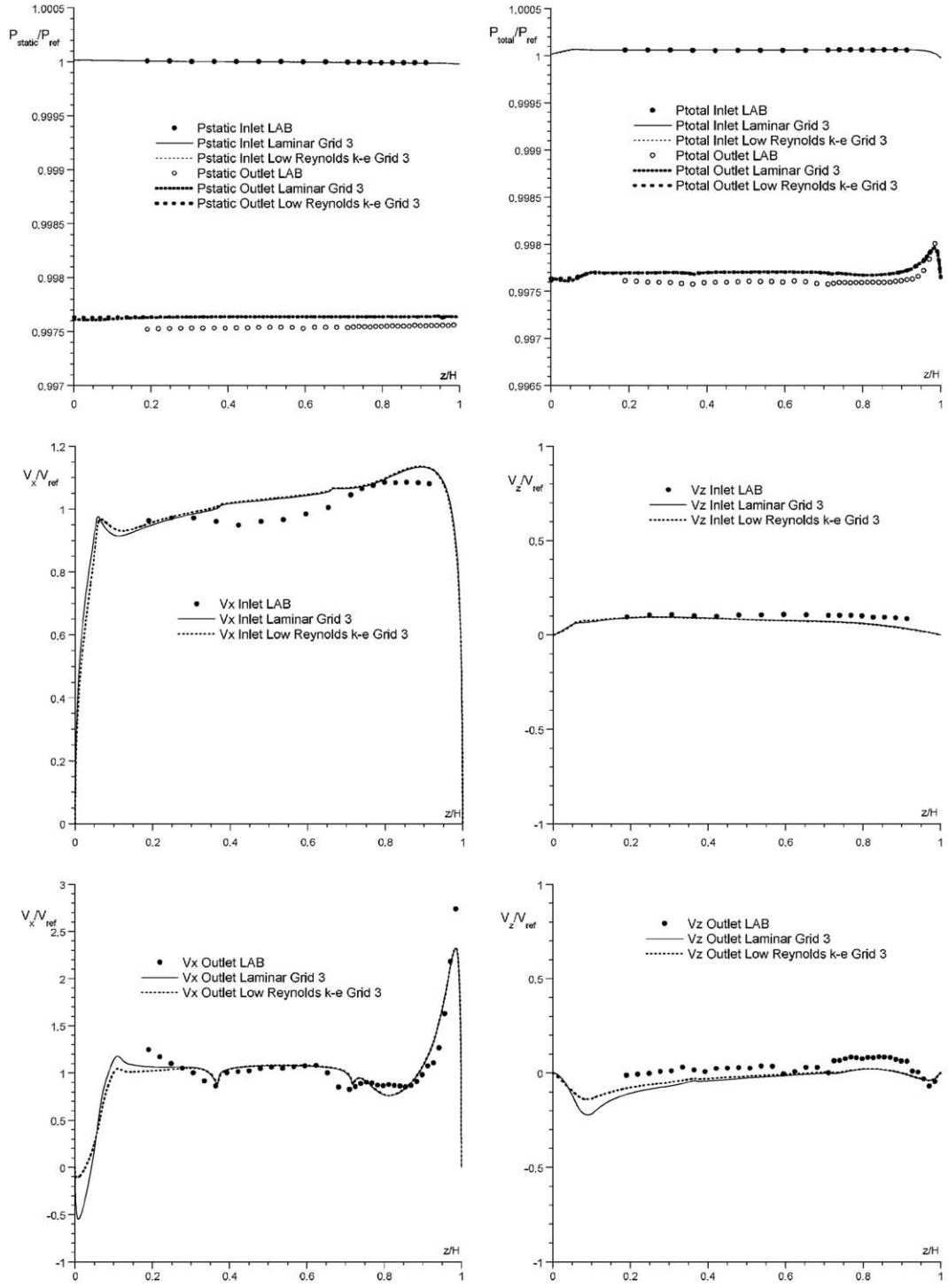

Fig. 17. Minimum inlet mass flow: comparative diagrams for the laminar and turbulent modeling with the experimental data and for the static/total pressure, velocity components at the inlet and outlet locations of the heat exchanger.

grid dependency studies led to the adoption of a grid for the flow modeling which had 96,554 computational nodes. In the final stage, two modeling approaches were performed with the aid of a commercial CFD package. The two approaches consisted of a laminar and a turbulent one separately, in order to check which of the two could predict better the flow development. The indication for this action resulted from the fact, that for the majority of the inlet mass flows, the transitional Reynolds numbers were closer to the values corresponding to the laminar regime of the flow. The computational results showed better agreement with the experimental measurements when a laminar modeling was performed, although there were regions in the experimental setup

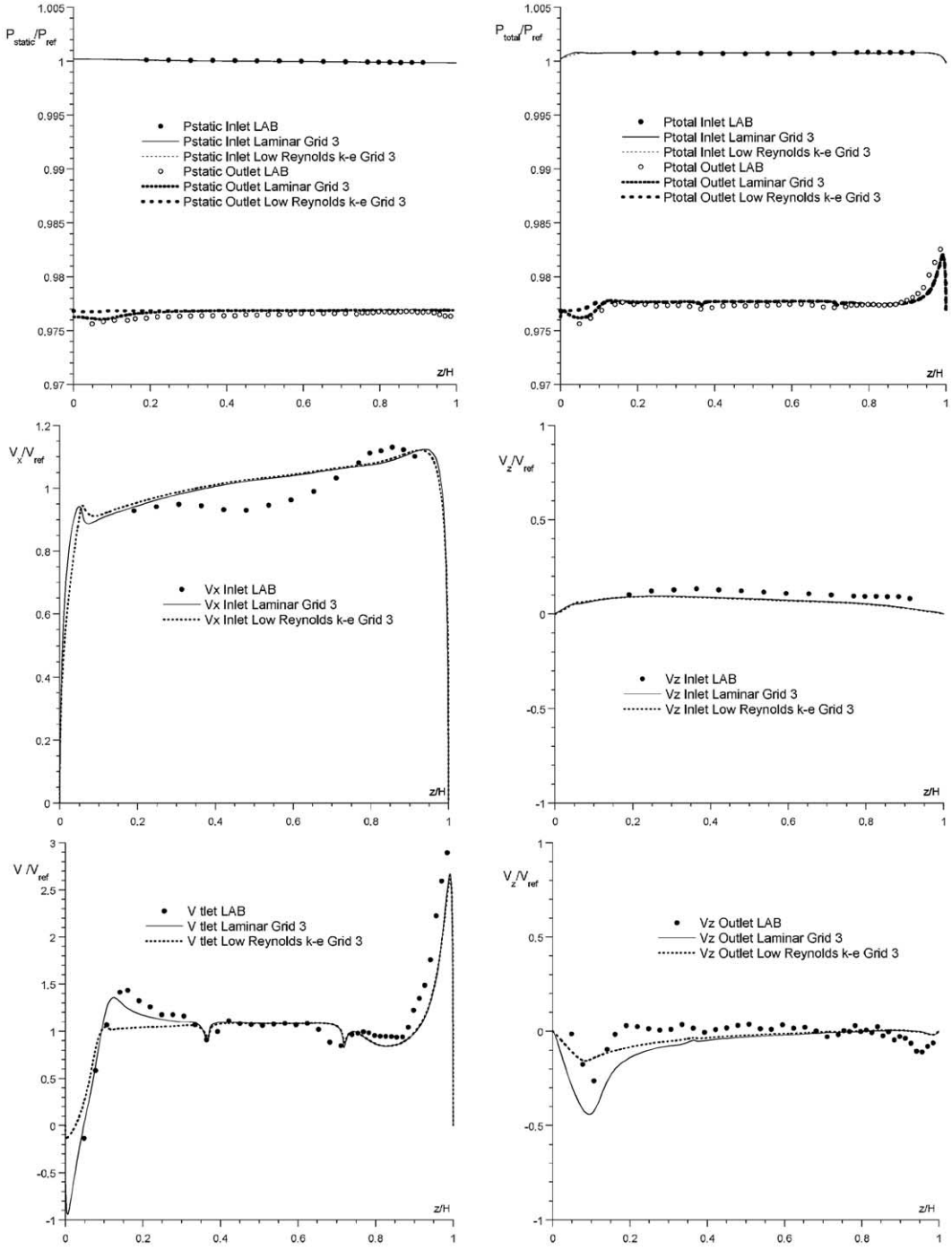

Fig. 18. Maximum inlet mass flow: comparative diagrams for the laminar and turbulent modeling with the experimental data and for the static/total pressure, velocity components at the inlet and outlet locations of the heat exchanger.

where the values of the measured turbulence intensity were relatively high such as the region located at the exit of the test section (downstream the heat exchanger) with average values up to 5.8%. This observation was clearly shown and supported by the flow development in the regions behind the cylindrical pipes of the collector where a large separation region occurred. The turbulent computations underpredicted the size of this zone in all cases. Unfortunately, there is no straight answer if someone should proceed with a turbulent or a laminar approach for the modeling of alternative designs, such as the one presented in this work. The chosen low-Reynolds-number turbulence model of Launder and Sharma, is a model widely used in the industry, although it has been found to have some major deficiencies. For the specific case of the underprediction of the separation

zone in the cylindrical pipes, many explanations could be offered. First of all, the computational modeling was 2D, although the problem is a 3D one. In the real case, there are three velocity components contributing to the flow field development. The third component is not taken into account. Additionally, the separation region formed in the curved surface of the cylinder belongs to a flow region where an adverse pressure gradient is imposed (due to the cylinder's curvature, the flow is decelerating). It is well known in such cases that a typical k–ε model suffer of inaccuracy. In order to have a well supported answer to the main question, a more detailed numerical investigation should be performed by testing a number of widely used turbulence models. And this should be combined with a further detailed modeling of this specific transitional flow.

Through this work, it has been well understood that further detailed modeling for this specific transitional flow development through a heat exchanger must be performed using more sophisticated extended turbulence models. Additionally, the porous medium model derived here must be checked in alternative flow configurations through the heat exchanger, such as the ones having different angles of attack for the main streamwise velocity component or different inlet turbulence intensities.

Acknowledgments

A major part of this work has been financially supported by the E.U. under the "Competitive and Sustainable Growth Programme", contract no. G4RD-CT-1999-00069. The authors would like gratefully acknowledge the support of Dr. R. Dunker, scientific officer of the project.

References

Boetler, L.M.K., Guibert, A.G., Romie, F.E., Sanders, V.D., Rademacher, J.M., 1949. An investigation of aircraft heaters XXXI—Summary of laboratory testing of several exhaust-gas and air heat exchangers. University of California, National Advisory Committee for Aeronautics, Technical Note 1455.

Bordalo, S.N., Saboya, F.E.M., 1999. Pressure drop coefficients for elliptic and circular sections in one, two and three row arrangement of plate fin and tube heat exchangers. J. Braz. Soc. Mech. Sci. XXI (4), 600–610.

Bouris, D., Papadakis, G., Bergeles, G., 2001. Numerical evaluation of alternate tube configurations for particle decomposition rate reduction in heat exchanger tube bundles. Int. J. Heat Fluid Flow 22, 525–536.

Brauer, H., 1964. Compact heat exchangers. Chem. Process Eng., 451–460.

FINE™ Numeca's Flow Integrated Environment. User Manual, ver. 5.2, June 2001.

Goulas, A., Katheder, K., Palikaras, A., Yakinthos, K., 2003. Flow measurements and investigations in a staggered tube matrix of a heat exchanger. Int. J. Heat Technol. 21 (2).

Kays, W., London, A., 1984. Compact Heat Exchangers, third ed. McGraw Hill, New York.

Matos, R.S., Vargas, J.V.C., Laursen, T.A., Saboya, F.E.M., 2001. Optimization study and heat transfer comparison of staggered circular and elliptic tubes in forced convection. Int. J. Heat Mass Transfer 44, 3953–3961.

Morrison, G.L., Schobeiri, M.T., Pappu, K.R., 1998. Five-hole pressure probe analysis technique. Flow Measure. Instrument. 9, 153–158.

Rocha, L.A.O., Saboya, F.E.M., Vargas, J.V.C., 1997. A comparative study of elliptical and circular sections in one and two row tubes and plate fin heat exchangers. Int. J. Heat Fluid Flow 18, 247–252.

Saboya, S.M., Saboya, F.E.M., 2001. Experiments on elliptic sections in one and two row arrangements of plate fin and tube heat exchanger. Experiment. Therm. Fluid Sci. 24, 67–75.

Savill, A.M., 2002. By-pass transition using conventional closures, closure strategies for turbulent and transitional flows. In: Launder, B.L., Sandham, N. (Eds.), Cambridge University Press.

Schönenborn, H., Simon, B., Ebert, E., Storm, P., 2004. Thermomechanical design of a heat exchanger for a recuperative aero engine. In: Proceedings of ASME Turbo Expo 2004, Power for Land, Sea and Air.

Schulenberg, F., 1966. Finned elliptical tubes and their applications in air-cooled heat exchangers. J. Eng. Ind. 88, 179–190.

Umeda, S., Yang, S.W., 1999. Interaction of von Karman vortices and intersecting main streams in staggered tubes bundles. Experiments in Fluids 26, 389–396.

Yasar Gundogdu, M., Carpinlioglu, Melda O., 1998. A multi-tube pressure probe calibration method for measurements of mean flow parameters in swirling flows. Flow Measure. Instrument. 9, 243–248.